Dislocation Hardening in a New Manufacturing Route of Ferritic Oxide Dispersion-Strengthened Fe-14Cr Cladding Tube

Freddy Salliot, András Borbély, Denis Sornin, Roland E Logé, Gabriel Spartacus, Hadrien Leguy, Thierry Baudin, Yann de Carlan

Article

Dislocation Hardening in a New Manufacturing Route of Ferritic Oxide Dispersion-Strengthened Fe-14Cr Cladding Tube

Freddy Salliot [1,*], András Borbély [2], Denis Sornin [1], Roland Logé [3], Gabriel Spartacus [4], Hadrien Leguy [1], Thierry Baudin [5] and Yann de Carlan [1]

[1] Université Paris-Saclay, CEA, Service de Recherche en Matériaux et Procédés Avancés, 91191 Gif-sur-Yvette, France; yann.decarlan@cea.fr (Y.d.C.)
[2] Mines Saint-Etienne, Univ. Lyon, CNRS, UMR 5307 LGF, Centre SMS, F-42023 Saint-Etienne, France; borbely@emse.fr
[3] Thermomechanical Metallurgy Laboratory (LMTM)—PX Group Chair, École Polytechnique Fédérale de Lausanne (EPFL), CH-2002 Neuchâtel, Switzerland; roland.loge@epfl.ch
[4] Department of Materials Science and Engineering, KTH Royal Institute of Technology, SE-100 44 Stockholm, Sweden; spartac@kth.se
[5] Université Paris-Saclay, CNRS, Institut de Chimie Moléculaire et des Matériaux d'Orsay, 91405 Orsay, France; thierry.baudin@universite-paris-saclay.fr
* Correspondence: salliot.freddy@gmail.com

Abstract: The microstructure evolution associated with the cold forming sequence of an Fe-14Cr-1W-0.3Ti-0.3Y$_2$O$_3$ grade ferritic stainless steel strengthened by dispersion of nano oxides (ODS) was investigated. The material, initially hot extruded at 1100 °C and then shaped into cladding tube geometry via HPTR cold pilgering, shows a high microstructure stability that affects stress release heat treatment efficiency. Each step of the process was analyzed to better understand the microstructure stability of the material. Despite high levels of stored energy, heat treatments, up to 1350 °C, do not allow for recrystallization of the material. The Vickers hardness shows significant variations along the manufacturing steps. Thanks to a combination of EBSD and X-ray diffraction measurements, this study gives a new insight into the contribution of statistically stored dislocation (SSD) recovery on the hardness evolution during an ODS steel cold forming sequence. SSD density, close to 4.10^{15} m^{-2} after cold rolling, drops by only an order of magnitude during heat treatment, while geometrically necessary dislocation (GND) density, close to 1.10^{15} m^{-2}, remains stable. Hardness decrease during heat treatments appears to be controlled only by the evolution of SSD.

Keywords: ODS steel; microstructure; cold rolling; dislocation density; X-ray diffraction; EBSD

1. Introduction

The development of the fourth generation of nuclear reactors is in progress world-wide. This generation meets the requirements of closing the lifecycle of nuclear fuels [1] while improving efficiency and safety. Thanks to substantial feedback since 1951 with the first reactor EBR-1 (Idaho), the sodium-cooled fast reactor (SFR) is the most advanced design. In this architecture, the reactor core environment is more severe than in a pressurized water reactor. Parts inside the core are subjected to neutron flux, causing more than 200 dpa, and operation in temperatures up to 650 °C [2,3].

Oxide dispersion strengthened (ODS) steels were identified in the 1960s as promising candidates for SFR cladding tubes [4], and also for the first wall in fusion reactors. Indeed, the body-centered cubic matrix provides favorable resistance for creep and swelling under irradiation, and the homogenous dispersion of nano-oxides increases the mechanical properties at high temperatures. The high chromium content in ferritic steels (>12 wt %) confers a better corrosion resistance compared to martensitic ones, but lowers the manufacturability.

Ferritic steel claddings are commonly shaped by cold working like pilgering to benefit from better geometrical accuracy [5–11]. Forming them is challenging since hardness higher

than 400 HV1 may cause cladding cracks [7–12]. The absence of phase transformation in ferritic steel grade manufacturing requires high temperature intermediate heat treatments in order to soften and recover the material between the pilgering steps. Because of cold pilgering, grains are morphologically elongated along the rolling direction (RD). Also, the <110> lattice directions become aligned with the RD (α fiber) [13]. These microstructural and textural anisotropies influence mechanical properties, inducing a higher strength [14–16].

Microstructures of ODS grades are very sensitive to the chemical composition. Ukai et al. [14] concluded that a content of Y_2O_3 lower than 0.25 wt % leads to a recrystallized microstructure after specific heat treatment. This result has been confirmed by other studies [5,17] on $Fe–12Cr–1.5W–0.26Ti–0.22Y_2O_3$ cold-rolled tubes. However, the grade $Fe–15Cr–2W–0.3 Y_2O_3$ that presents a higher Y_2O_3 content also exhibits a recrystallized microstructure [18]. Quantitative data on dislocation densities and their evolution in microstructures have been little studied through recrystallization problematics.

This study highlights the microstructural stability of an Fe-14Cr (Fe-14Cr-1W-0.3Ti-0.3 Y_2O_3) ODS cladding tube during manufacturing. The investigated material is similar to 14YWT, which after extrusion at 850 °C, exhibits the ability to recrystallize as described in the standard CEA (The French Atomic Energy and Alternative Energy Commission) protocol in [8].

The newly proposed process route has been designed with two variations compared with the standard one: (i) a higher cumulated cross section reduction ratio than in [7] by using two successive passes and (ii) a removed stress release treatment compared to [7,8]. None of these changes, which allow for a higher stored energy, led to the recrystallization of the material.

Several microstructural indicators were analyzed, such as nano-oxides volume fraction, grain size, crystallographic texture and geometrically necessary dislocation (GND) densities from EBSD to understand hardness variation through the steps. In addition, X-ray line profile analysis (LPA) has been used to investigate the impact of stress release treatment on dislocation density.

2. Materials and Methods

2.1. Materials and Shaping

This paper focuses on an $Fe-14Cr-1W-0.3Ti-0.3Y_2O_3$ grade steel obtained by powder metallurgy. In this process, a pre-alloyed ferritic matrix powder (Fe, Cr, W, Mn, Ni, . . .) atomized by Aubert & Duval was ball-milled with powders of Y_2O_3 and TiH_2 by Plansee. Then, the powders were consolidated by hot extrusion. For this grade, powders and mother tube were manufactured with the same parameters as in a previous study of Toualbi et al. [7]. The processing route was designed with moderate straining by cold rolling passes (with a cumulated logarithmic reduction ratio of ~40%) and intermediate heat treatment of 60 min at 1200 °C (Figure 1). The samples were named according to the rolling pass number followed by "b" or "a", respectively, for "before" and "after" heat treatment. Total strain ε_{tot} is defined as the logarithmic ratio of the surfaces before and after rolling.

Heat treatments were performed under He atmosphere to strictly limit steel oxidation. Temperature and heating rates were monitored during heat treatment. Cooling rates were not analyzed, since they affect neither oxide precipitation nor the microstructure of ferritic steel. Ultimately, the mother tube was cold pilgered via high-precision tube rolling (HPTR) down to 500 μm wall thickness. The chemical composition is given in Table 1.
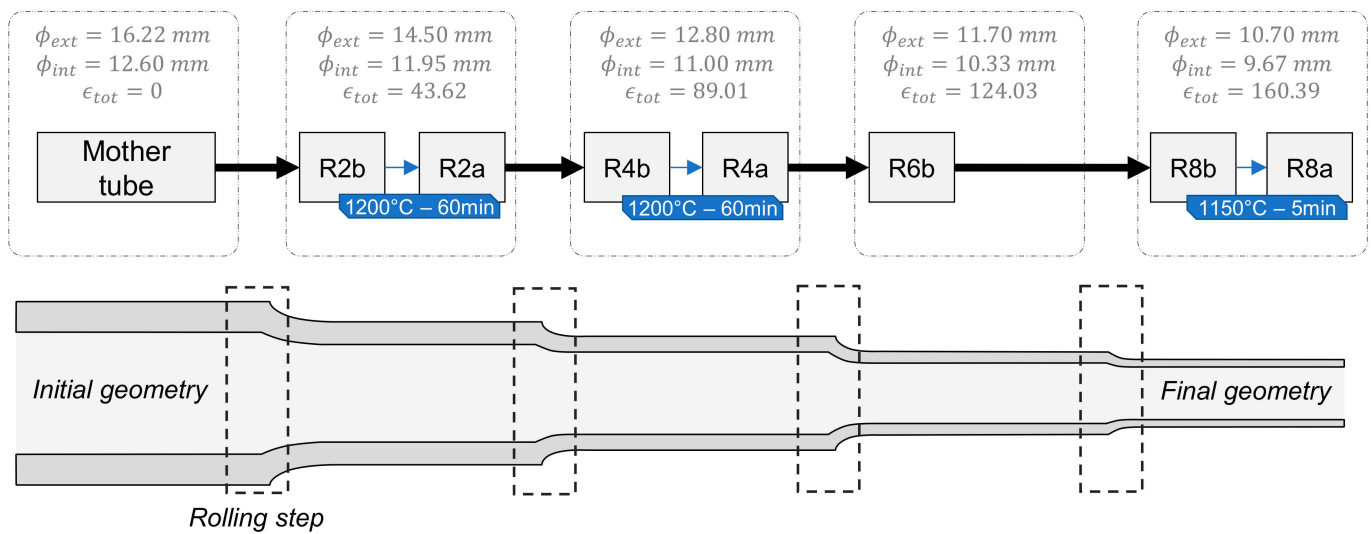
**Figure 1.** Denomination of the tube states during the rolling process.

Table 1. Chemical composition of Fe-14Cr studied grade. The carbon content is obtained by combustion with infrared detection, the nitrogen content by reductive fusion–thermal conductivity and the oxygen content by reductive fusion–infrared absorption. All other contents are measured by plasma emission spectrometry.

Content (wt.%)											
Fe	C	Cr	Mn	Mo	Ni	Si	Ti	W	Y	N	O
Bal.	0.013 ±0.001	14 ±0.6	0.25 ±0.02	0.005 ±0.001	0.33 ±0.05	0.28 ±0.01	0.27 ±0.01	1.1 ±0.27	0.15 ±0.04	0.015 ±0.0005	0.13 ±0.01

2.2. Experimental Techniques

All analyzed samples were taken from one cladding tube, extracted after each step of the shaping process.

Vickers hardness tests were performed using an Innovatest Falcon 500 durometer with 1 kgf load on the longitudinal [RD, normal direction (ND)] plane (Figure 2). Samples were polished until mirror surface finishing (with 1 μm diamond paste) prior to hardness testing.
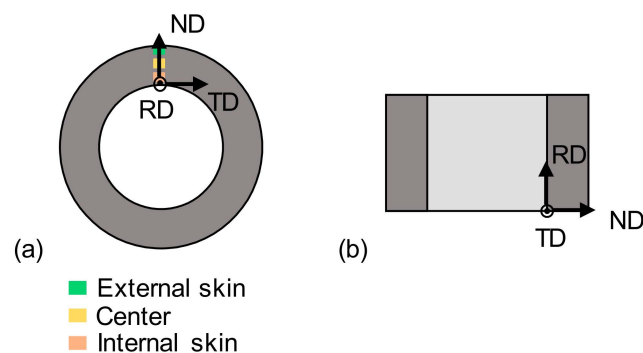
Figure 2. (**a**) Transverse section with the zones of interest; (**b**) longitudinal section.

Microstructural and texture characterizations were made via EBSD. Data were acquired using an SEM-FEG Zeiss SIGMA HD equipped with an Oxford fast EBSD detector, and were analyzed with the EDAX-OIM V8 software. The final preparation of EBSD samples was an electrochemical polishing that removes the hardened layer induced by diamond polishing. Orientation maps were acquired on the transverse [ND, transverse direction

(TD)] plane to analyze more grains near the external skin where deformation amount is greater (Figure 2). Orientation maps were acquired with 20 kV acceleration voltage and a 35 nm step size on 21×28 μm^2 area size. Texture calculations were performed using the generalized spherical harmonic series expansion approach. Calculations were performed with 34 coefficients and a 5° Gaussian half width.

Small-angle X-ray scattering (SAXS) experiments were performed on ODS steels to characterize the nano-sized oxide dispersion in the ferritic matrix. Following the same parameters as a similar study [19], data were acquired using a laboratory setup at CEA (Saclay). A Mo anode X-ray source was used (wavelength of 0.07107 nm) with a beam size of ~1 mm^2. Samples were polished down to 80 μm thickness according to the beam energy to obtain sufficient transmission signal (10–20% of the incident intensity). The beam was aligned with ND and passed through the whole thickness of the tube.

Each SAXS measurement consisted of a two-dimensional pattern, which was azimuthally integrated, background subtracted and normalized by the incident flux, specimen thickness, transmission and solid angle viewed by the detector. Intensity was reduced to absolute units using a glassy carbon secondary standard (NIST-SRM 3600 [20]). To extract the mean radius and volume fraction, the SAXS data were fitted by a model described in [21], taking into account a lognormal distribution of spheres with a dispersion of 20% [22]. More calculation details are available in [23,24].

X-ray diffraction (XRD) patterns were acquired at the beam line P21.2 of the Petra III–DESY synchrotron (Hamburg). The X-ray energy was 83 keV, and a beam size of 150×150 μm^2 was used. The beam was aligned with ND and passed through the whole thickness of the tube. A Linkam TS1500V oven heated the sample up to 1200 °C at a rate of 200 °C/min. For evaluation, the 2D XRD patterns were azimuthally integrated. The instrumental broadening was measured with a NIST LaB6 standard (SRM 660a). The modified Warren–Averbach method (mWA) was used to estimate dislocation density as described in [25]. The mWA method links the amplitude of the Fourier coefficients $A(n)$ of the line profile to the dislocation density ρ following Equation (1).

$$\ln(A(n)) \cong A^S(n) - \rho B n^2 \ln\left(\frac{R_e}{n}\right)\left(K^2 C\right) + Q B^2 n^4 \ln\left(\frac{R_1}{n}\right) \ln\left(\frac{R_2}{n}\right)\left(K^2 C\right)^2 \quad (1)$$

where $A^S(n)$ is the small crystallite size contribution to broadening [25], n is the Fourier parameter, and $B = \pi b^2/2$ with b as the magnitude of the Burgers vector. R_e is the outer cut-off radius (or screening length) of the dislocation ensemble, while R_1 and R_2 are parameters with length dimension, but no physical interpretation.

$K = 2\sin(\theta)/\lambda$, with λ as the X-ray beam wavelength and θ as the Bragg angle. The dislocation contrast factor C of each diffraction peak was calculated with ANIZC using theoretical elastic constants for a ferromagnetic Fe-Cr alloy at 15 at.% Cr [26] and the assumption that edge and screw dislocations are present in equal proportion. The factor $Q = \left(\overline{\rho^2} - \overline{\rho}^2\right)/2$ represents the fluctuation of the dislocation density.

It was shown recently that the full width at half maximum (FWHM) of the peaks is strongly influenced by the arrangement of dislocations [27], and this broadening better approximates the stored energy than the value which considers R_e evaluated from Equation (1) [28]. Its physical reason relies on the fact that Equation (1) is the asymptotic approximation of the Fourier transform of the peak profile valid at small n, which is in contradiction with the long-range interaction length between dislocations that determines their screening distance. For example, for a system of randomly arranged edge dislocation dipoles, the value of R_e obtained from Equation (1) overestimates the true screening length by one order of magnitude [27]. Therefore, the strain energy and the corresponding screening length R_e was evaluated using the modified Williamson–Hall method (mWH):

$$\Delta K = \left(\frac{A_D}{D}\right) + \left[\frac{b^2}{4\pi}\rho \ln\left(\frac{R_e}{r_0}\right)\right]^{1/2} K\sqrt{C} + O\left(K\sqrt{C}\right)^2 \quad (2)$$

where $K = 2\sin(\theta)/\lambda$, $\Delta K = FWHM\cos(\theta)/\lambda$, and the inner cut-off radius r_0 was taken to be equal to 2.6 b [29].

3. Results and Discussion

3.1. Hardness Evolution during the Manufacturing Route

The processing route was designed at CEA to reduce the mother tube (MT) to the final section by cold rolling, without damaging the tube by crack formation. The various intermediate steps are referenced in Figure 1. The total strain ε_{tot} and associated hardness values are drawn in Figure 3. Obviously, each pilgering step implies hardening, while each heat treatment softens the material.
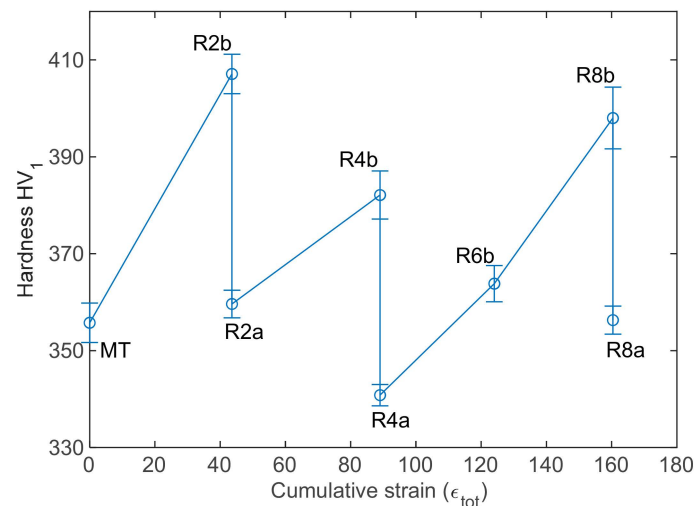
Figure 3. Vickers hardness at each step of the process.

3.2. Microstructural Evolution

3.2.1. Nano-Oxides

SAXS has been used to measure nano-oxide size and volume fraction evolutions. Samples with α fiber texture were analyzed with the RD aligned with the X-ray beam direction to avoid an elliptic SAXS pattern related to the material texture. The assumption was made that $Y_2Ti_2O_7$ pyrochlore was the only nano-oxides phase for the estimation of the volume fraction (f_V), as it is the most commonly identified phase in the literature [30,31]. R8* is a sample similar to R8a with a 750 °C, 30 min long heat treatment. Results are displayed in Table 2 and show a slight increase in the nano-oxide mean radius (R_m) during the manufacturing from 1.4 nm to 2.0 nm. Taking into account the thermal history of consolidation and extrusion of the material to obtain the MT state, the initial radius obtained is in agreement with radius observed or calculated in [21,32] after heating up to 1100 °C.

Table 2. Volume fraction and mean radius of $Y_2Ti_2O_7$ nano-oxides calculated from SAXS signal. Standard deviation is linked to the calculated dispersion. R8* is a sample similar to R8a with a 750 °C, 30 min long heat treatment.

	MT	R2a	R8*
Volume fraction (%)	0.36 ± 0.09	0.33 ± 0.08	0.26 ± 0.07
Mean radius (nm)	1.4 ± 0.2	1.8 ± 0.2	2.0 ± 0.1

The growth of the nano-oxides is most likely due to coalescence during the successive thermal treatments, as the volume fraction seems to remain constant. The mean radius variations remain small, as $Y_2Ti_2O_7$ pyrochlore is known to exhibit a strong stability against coarsening even at a high temperature [33]. Knowing that nano-oxide density N can be

calculated with Equation (3), it comes to N $\approx 10^{23}$–10^{24} m^{-2}, in agreement with previous TEM observations [31].

$$N = \frac{f_V}{\frac{4}{3}\pi R_m^3} \tag{3}$$

This high density exerts high Zener pressure at every step of the manufacturing, and is responsible for grain boundary and dislocation pinning [34].

### 3.2.2. Grain Size, Texture and Dislocation Density

EBSD is a powerful method to extract microstructure and texture data from orientation maps. Analyses were performed on each step of the forming process on the [ND, TD] section to characterize their evolutions. The grain boundary was defined by considering a disorientation greater than $10°$. The grain size was mostly below a 5 μm equivalent diameter (D) with a non-Gaussian distribution. So, three grain populations were studied to compare microstructures: D < 0.5 μm, D > 1 μm and the population between. Figure 4 depicts these three population variations through a shaping route. The mean equivalent diameter is also given as a comparative tool. Bigger grains (D > 1 μm) decreased in number but also in area fraction, meaning bigger grains were subdivided during the whole process. Thus, smaller grains (D < 0.5 μm) doubled in number and their area fraction increased after each cold rolling pass, impacting the mean grain size of the cladding. Microstructure tends to be more fine-grained when adding deformation cycles (Figure 5).
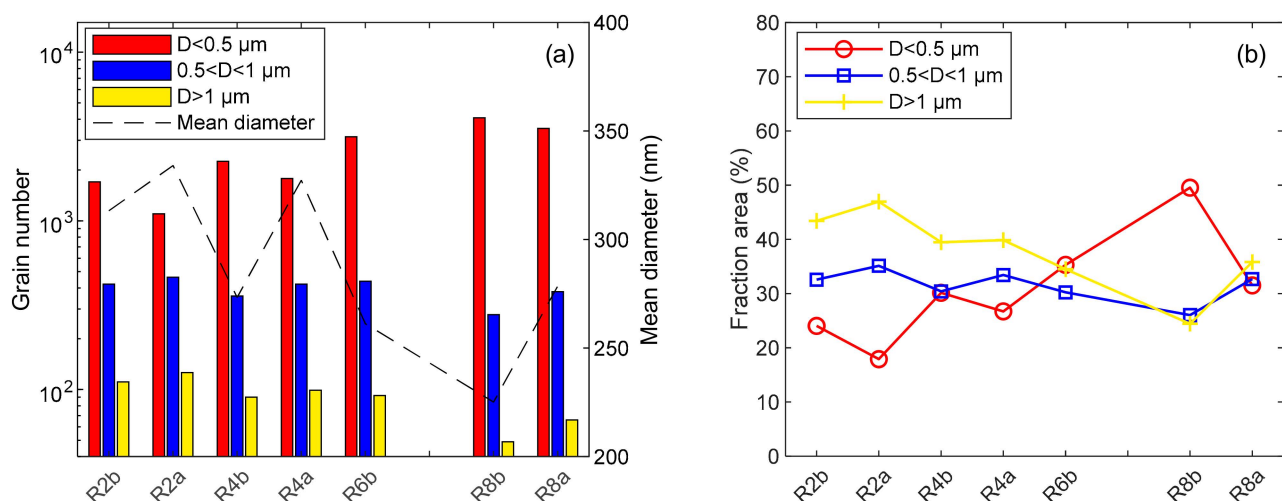
Figure 4. Evolution of mean diameter and grain populations in [ND, TD] section, near external skin through shaping process (**a**) in number; and (**b**) in area fraction.

Body-centered cubic (BCC) materials are well known to develop α fiber texture during rolling. The corresponding grains have crystallographic directions <110> aligned with RD [34]. This fiber is induced by extrusion [35] and is reinforced by pilgering. Regarding the outer skin, the fiber remains complete throughout the process (Figure 5) with a {111}<110> reinforcement. However, the preferential orientation tends to shift towards the {112}<110> orientation through the steps. These small and elongated (in RD) morphologies are not the most favorable for creep strength [36], but even heat treatments at 1250 °C, at whatever moment in the fabrication route, do not recrystallize the microstructure.

The texture evolution is consistent with previous work [37,38], which evidenced the formation of a strong incomplete fiber (between {001}<110> and {111}<110>) during cold rolling of different BCC materials. Raabe and Lücke [37] report, in the case of low-carbon steels, a dominance of the fiber components {001}<110> and {112}<110>.
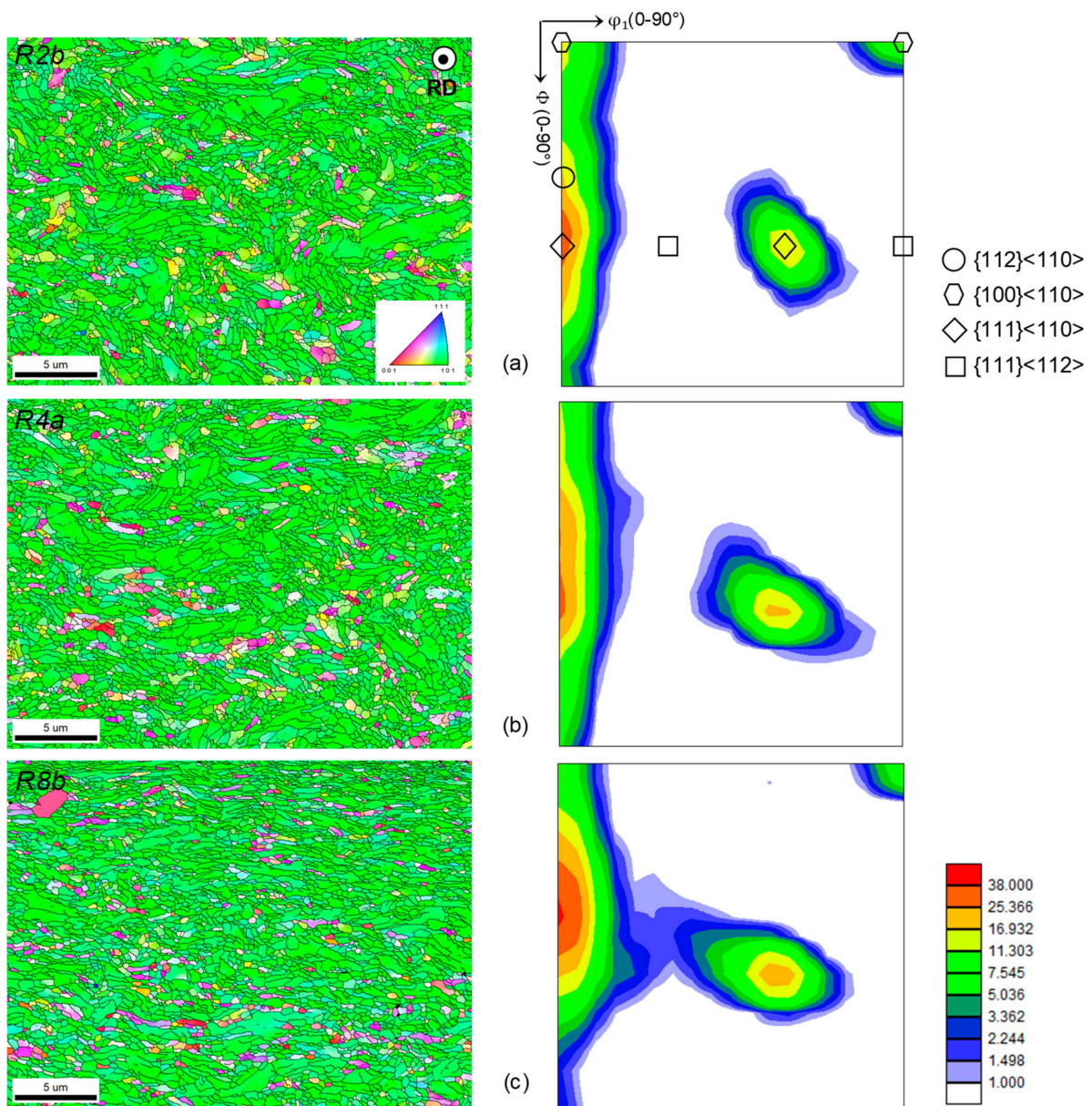
Figure 5. RD—IPF on TD plane on left side and Euler section at $\varphi_2 = 45°$ at external skin on right side for (**a**) R2b, (**b**) R4a and (**c**) R8b steps.

EBSD can also be used to calculate the geometrically necessary dislocation (GND) density [39]. Ashby [40] differentiates GNDs as dislocations tilting the crystal lattice to accommodate plastic strain and statistically stored dislocations (SSDs), which are randomly trapped dislocations that do not affect the orientation of the crystal lattice. So, only GND can be detected by conventional EBSD, and the lattice curvature is used to obtain their density ρ_{GND}. In this study, the Nye's tensor has been evaluated with the first neighbor, according to the method described in [41].

The evolution of average ρ_{GND} over the manufacturing process was evaluated at the center, at the internal skin and at the external skin of the tube and is presented in Figure 6. The error bars correspond to the standard deviation. ρ_{GND} stays mostly constant and high (~$1 \cdot 10^{15}$ m^{-2}). No clear fluctuation was found between the three sites, but low variation can be considered between the deformation and heating steps, even if those variations remain significantly lower than the error bars.
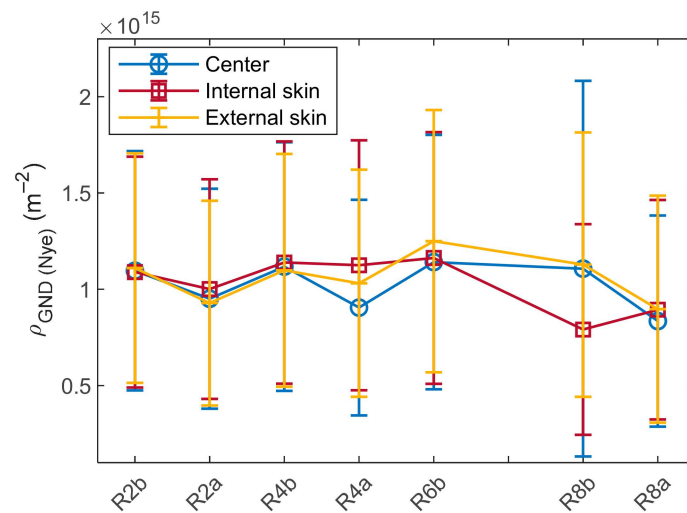
Figure 6. Average GND densities during the shaping process calculated by Nye's tensor method for different sites.

3.2.3. Hardening Contributions

Studied microstructural parameters are well known to contribute to the yield strength, and their contributions are usually added $\sigma_{YS} = \sigma_0 + \sigma_{SS} + \sigma_{GB} + \sqrt{\sigma_P^2 + \sigma_D^2}$ with σ_0 as the Peierls–Nabarro's stress, σ_{SS} as the solid solution contribution, σ_{GB} as the contribution of grain boundaries, σ_P as that of nanoparticles and σ_D as the dislocation hardening [42,43]. According to Tabor [44], "the Vickers hardness is equal to the flow stress of a test specimen after it has been plastically strained an additional 8%". Also, σ_{YS} has been experimentally found to be proportional to the hardness [45], with σ_{YS} (MPa) = hardness (MPa)/3 (1 HV$_1$ = 9.81 MPa).

σ_0 was calculated according to the Peierls–Nabarro equation:

$$\sigma_0 = M\frac{2\mu}{1-\nu}\exp\left(\frac{-2\pi a}{b(1-\nu)}\right) \tag{4}$$

where M is the mean Taylor factor (M = 2.5 for textured material), and μ and ν are the shear modulus (81 GPa) and the Poisson's ratio (0.3), respectively. a and b are, respectively, the lattice parameter and the modulus of the Burgers vector. σ_0 = 18 MPa in this study.

σ_{SS} was estimated based on the Lacy and Gensamer relation [46] $\sigma_{SS} = \sum_i k_i X_i^Z$. k_i and X_i are, respectively, the atomic concentration and the hardening constant associated with each atom i. The exponent Z depends on the nature of the element in solution. It is 0.5 for insertion elements and 0.75 for larger elements in substitution. σ_{SS} was 145 MPa according to chemical composition (Table 1).

The nano-oxides contribution σ_P was estimated with the modified Orowan equation proposed by Martin [47]:

$$\sigma_P = \frac{0.81M\mu b}{2\pi(1-\nu)2}\ln\left(\frac{1}{b}\sqrt{\frac{2}{3}}R_m\right)\bigg/\sqrt{\frac{2\pi}{3f_V}R_m} \tag{5}$$

Using R_m and f_V values from Table 2 gives $\sigma_P(MT)$= 350 $\pm$ 61 MPa, $\sigma_P(R2a)$= 304 $\pm$ 52 MPa and $\sigma_P(R8^*)$ = 257 $\pm$ 42 MPa.

Regarding the previous microstructural indicators, only (i) grain boundary strengthening and (ii) work hardening are considered in micro-hardness variations, since the solid solution hardening and σ_0 are not expected to change. Moreover, σ_P evolution cannot lead to changes in the measured hardness.

(i) Concerning the grain boundaries, the Hall–Petch effect is well known to explain the dependency of the yield stress (or hardness) with grain size [48]. To overcome the

non-gaussian distribution of grain size, the Hall–Petch model modified by Srinivasarao et al. [49] was used.

$$\sigma_{GB} = 0.2\mu\sqrt{b} \sum_i f_i^{area} / \sqrt{D_i} \tag{6}$$

where f_i^{area} is the area fraction of grains with a diameter D_i. EBSD data were used to calculate σ_{GB}. Values are displayed in Figure 7. The grain boundary contribution to yield strength evolves similarly to hardness variations through all thermomechanical steps. σ_{GB} increases during pilgering steps (from MT to R2b) and decreases during annealing (from R8b to R8a). However, MT and R8a show similar hardness values (Figure 3) with a higher difference between $\sigma_{GB}(MT)$ and $\sigma_{GB}(R8a)$ than between successive steps $\sigma_{GB}(MT)$ and $\sigma_{GB}(R2a)$. Hardness evolution cannot be fully explained by the Hall–Petch law.
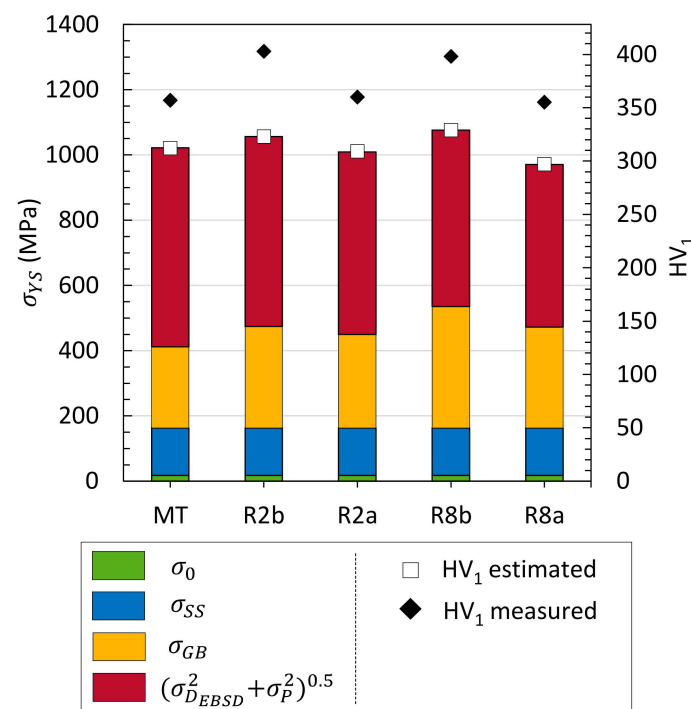
Figure 7. Estimated yield strength and hardness from microstructural contributions. Precipitate contribution $\sigma_P(R2b)$ is taken to be equal to $\sigma_P(MT)$ by assumption on a limited nano-oxide distribution evolution through cold pilgering step. The same for $\sigma_P(R8b)$, taken to be equal to $\sigma_P(R8a)$.

(ii) In pure face-centered cubic (FCC) crystals, the hardness is proportional to $\sqrt{\rho}$ through the Taylor's relation $\sigma_D = 0.3M\mu b\sqrt{\rho}$. For BCC phases like Fe-14Cr, this relation is not as clear as for FCC [50]. The GND density assessed by EBSD does not vary significantly (Figure 6), and considering their participation alone leads to estimation close to $\sigma_{D_{GND}}$ = 470 MPa (Figure 7). Many theoretical or experimental studies have been performed on FCC materials to correlate the amount of GND and SSD densities and their respective participation in work hardening, but no consensus has been found [40,50–53].

Finally, the GND density seems to saturate; however, it shows a very slight increase through pilgering steps, and a decrease upon heat treatment (Figure 6).

By considering all these microstructural contributions, the estimated hardness values are underestimated and do not fluctuate as much as the measured ones (Figure 7). This is particularly true for variations through heat treatment (from R2b to R2a, and from R8b to R8a). At this point, none of the microstructural contributions showed any significant variation, which could explain this evolution.

3.2.4. Heat Treatment Behavior

In order to characterize the microstructure stability at various temperatures, a thorough study has been performed on the sample corresponding to the last processing step R8b. In addition, samples were maintained at the desired temperature for different durations under a helium atmosphere, followed by helium quench. As no significant evolution was noticed on the grain size distribution, hardness was used to analyze the impact of heat treatment (Figure 8).
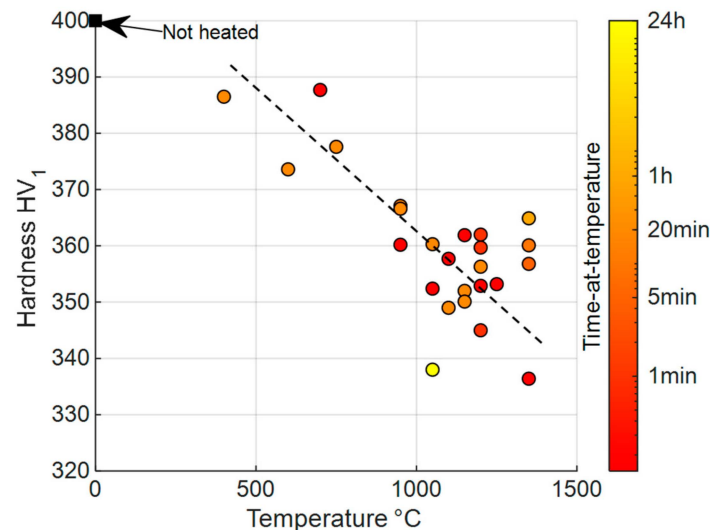

Figure 8. Hardness of R8b heated with various parameters.

First, little softening is noticed until 400 °C. Then, for higher temperatures, hardness can be considered as linearly decreasing with temperature. Finally, only the temperature seems to affect hardness at first order, without any variation in the microstructure observed by EBSD. Based on this result, heat treatments lasting less than a few hours can be wisely chosen in the manufacturing route to soften cladding before pilgering (Figure 8). Moreover, since extreme treatments (fast kinetics and low holding time) impact hardness as much as moderate ones, dislocation recovery is more likely to be responsible for a hardness decrease than slower mechanisms such as chemical diffusion. Since the GND density remains stable even after 5 min at 1150 °C (Figure 6), the SSD contribution must be considered.

The R8b sample was analyzed by XRD with the beamline of Petra III-DESY, in order to estimate the SSD density during heating. Considering the most severe treatment possible, the sample was heated at a rate of 200 °C/min, up to 1200 °C. The acquisition of diffraction patterns occurred every second. In situ obtained average diffractograms (integrated over the azimuthal angle of the 2D detector) at 55 °C and 1200 °C are shown in Figure 9. The decrease in the intensity at higher 2θ during heating was caused by the Debye–Waller effect. Due to its low intensity, the 222 peak was not taken into account in the analysis. The 110 peak contains more than 75% of counted photons due to the strong α fiber texture.

The dislocation density from the mWA analysis dropped from $3.8 \times 10^{15} \pm 1.2 \times 10^{14} \text{ m}^{-2}$ to $5.1 \times 10^{14} \pm 1.8 \times 10^{14} \text{ m}^{-2}$ during heating (Figure 10a). Since a density near 10^{13} m^{-2} is expected in recrystallized materials, it was concluded that only recovery occurs in the sample.
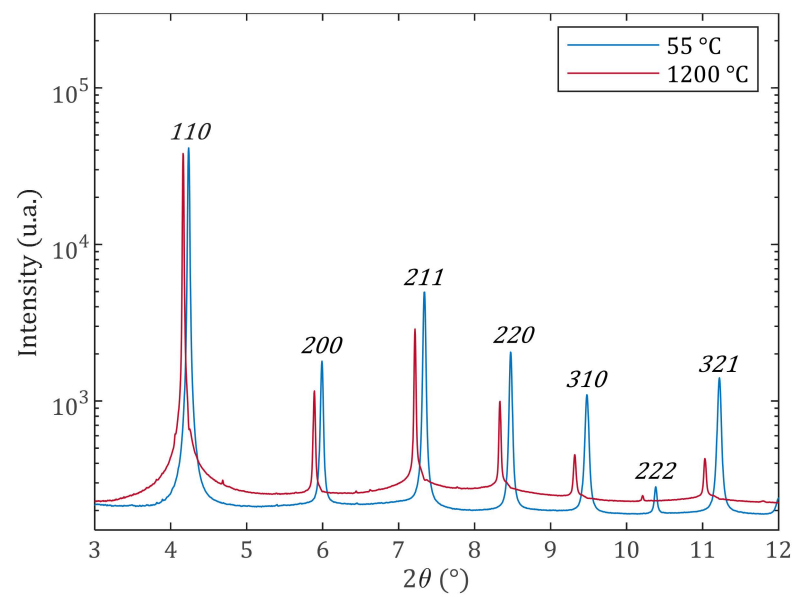
Figure 9. Average synchrotron X-ray diffractograms spectra measured on R8b at 55 °C and 1200 °C.
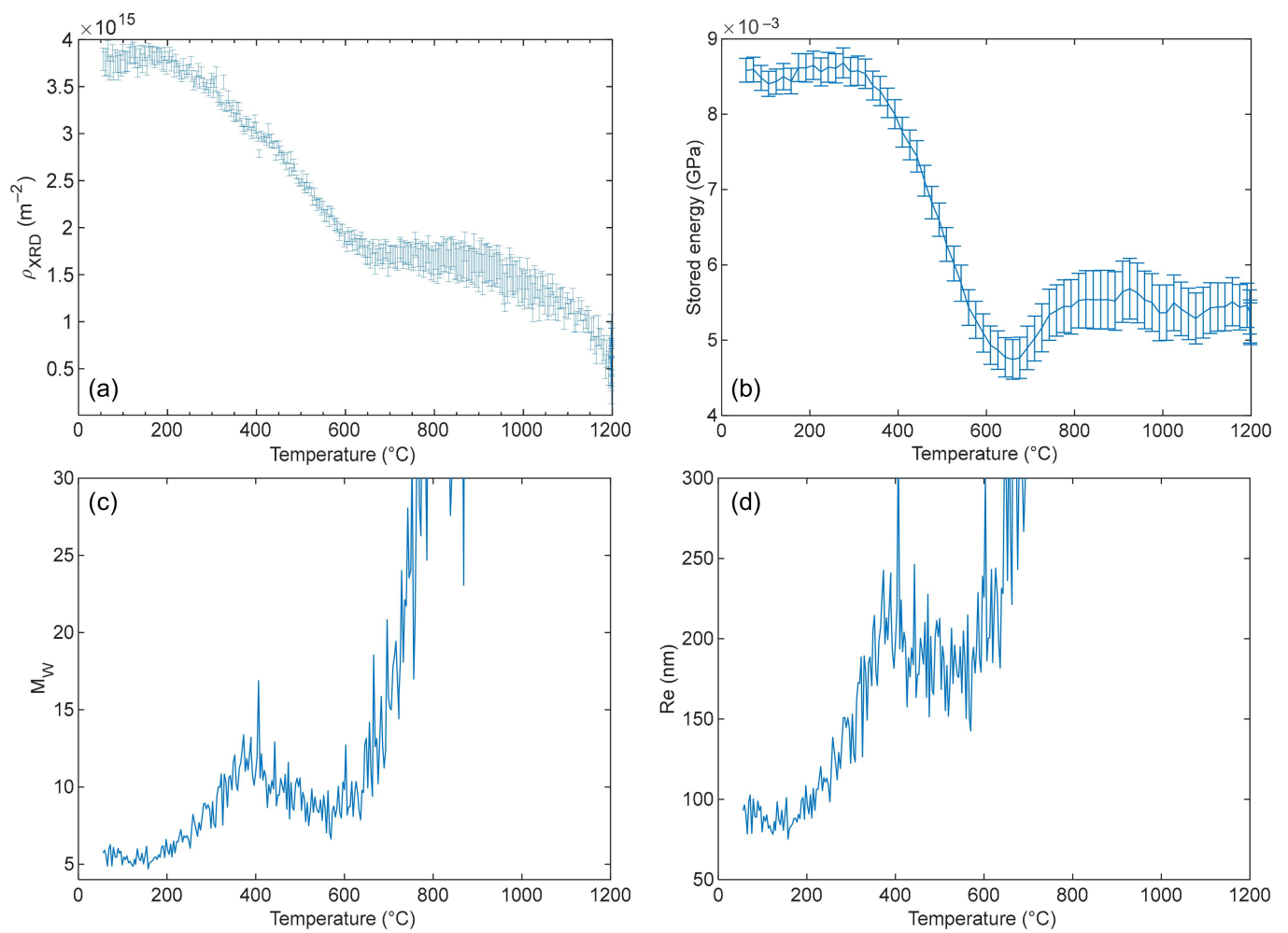
Figure 10. Evolution of (**a**) dislocation density, (**b**) stored energy, (**c**) the $M_W = R_e \sqrt{\rho_{XRD}}$ parameter, and (**d**) R_e during the heating from mWA and mWH calculations.

The stored energy (SE) takes into account the dislocation density but also the dislocation arrangement and can be directly obtained from the mWH plot [28]. Based on Figure 10a,b, the SE shows a similar behavior to the dislocation density. It remains stable from room temperature to about 300–400 °C, then both drop until 650 °C. Combining the SE values with the dislocation density given by the mWA method, the screening parameter R_e and the interaction parameter $M_W = R_e \sqrt{\rho}$ [54] can be calculated (Figures 10d and 10c, respectively).

- From room temperature to 400 °C, ρ_{XRD} decreases and M_W increases (Figure 10c). The latter describes the average dislocation [28]. The increase in both R_e and M_W can be understood in terms of the annihilation of dislocation dipoles for which R_e is small [28]. Although both the dipoles and sub-grain boundaries have a small M_W, the latter are stable structures at high temperatures, as seen before with ρ_{GND} evolution.
- From 400 to 600 °C, both ρ_{XRD} and M_W decline slightly. This means that SSD start to annihilate with a faster kinetics than bellow 400 °C. Since M_W and R_e are decreasing (Figure 10d), assumption can be made on the disappearance of dislocations with longer screening length. In addition, some dislocations can rearrange into GND structures (with lower energy), also leading to a decrease in M_W and R_e.
- The 650–700 °C temperature range corresponds to the sample Curie point measured by calorimetry for this sample. Anomalous behavior in the lattice parameters [55] and also in diffusion kinetics are well known around the Curie point in ferritic stainless steels. In the studied alloy, these changes are local and since the material did not transform completely to the FCC phase (small austenite peak is visible near the 110 refection above 800 °C, Figure 9), they could induce extra strain, affecting peak broadening. As the measurements were acquired during heating, crossing the Curie point, this anomalous behavior could lead to the observed increase in M_W and R_e, describing the dislocation rearrangement. The interpretation of these parameters above 600 °C is not possible. This austenitic phase disappears again after cooling.

Table 3 lists the dislocation density estimated from EBSD and mWA of the sample before heat treatment (R8b) and after heat treatment (R8a). Both XRD acquisitions were performed at 55 °C, and others were perfmored at room temperature. The GND density measured by EBSD was slightly reduced, while ρ_{XRD} was divided by about eight. This reduction can be attributed to SSD density.

Table 3. Dislocation density before and after heating up to 1200 °C at +200 °C/min obtained from EBSD and XRD (calculated with the mWA method).

	R8b	R8a
ρ_{EBSD} (10^{15} m^{-2})	1.0 ± 0.6	0.8 ± 0.5
ρ_{XRD} (10^{15} m^{-2})	3.8 ± 0.2	0.5 ± 0.2

Assuming that the nano-oxide distribution does not evolve during this relatively rapid heat treatment, the $\left(\sigma_{D\,total}^2 + \sigma_P^2\right)^{0.5}$ contribution was estimated, as well as the yield strength and Vickers hardness (Figure 11).

- Hardening models

Taking ρ_{XRD} into account results obviously in a greater variation in the estimated yield strength and, therefore, in the estimated hardness, than that with only GND. In the case of R8a (Figures 7 and 11), the estimated hardness goes from 297 HV$_1$ (EBSD) to 329 HV$_1$ (EBSD + XRD) for an experimental value of 355 HV$_1$. Thus, softening during annealing seems to be mainly controlled by SSDs in this highly strained and textured BCC material since the GND density does not evolve significantly.
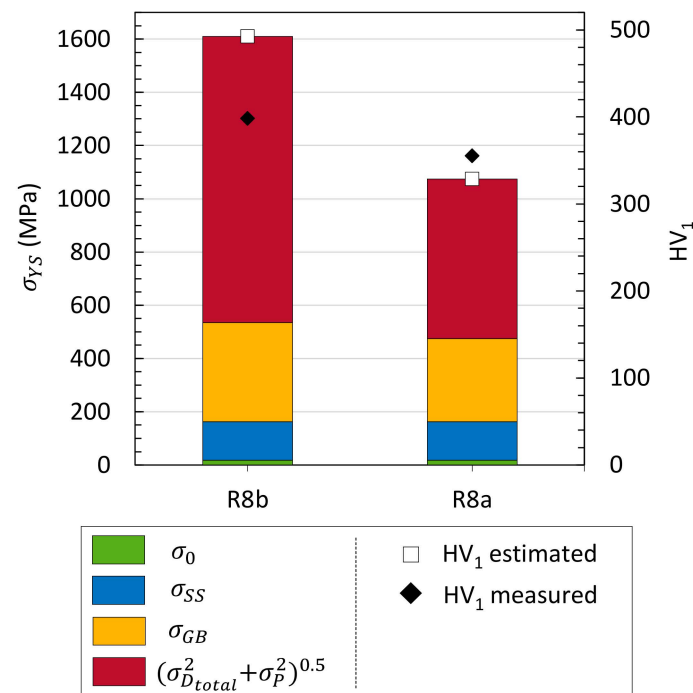
Figure 11. Estimated yield strength and hardness from complete microstructural contributions before and after heating up to 1200 °C at +200 °C/min. Precipitate contribution is taken constant.

Also, for R8b, the estimated hardness rises from 329 HV_1 (EBSD) to 492 HV_1 (EBSD + XRD) for an experimental value of 398 HV_1. Then, the yield strength (and hardness) is overestimated. This can be due to several approximations.

The Taylor's relation $\sigma_D = \alpha M \mu b \sqrt{\rho}$ seems not to be the right description for these materials since differences between the measured and estimated hardness values are still large. The average value of the Taylor factor M could be reconsidered (i) even though it has little impact on the estimates, as could the α-factor (ii) (here fixed at 0.3), which can vary if the dislocation structure changes [56,57]. Also, (iii) the total dislocation density may be underestimated. According to [28], the asymptotic mWA allows for a reliable evaluation of the dislocation density if the local distance between dislocations is larger than about 30 nm, which corresponds to a total dislocation density of 10^{15} m^{-2}. This means that in the case of Fe-14Cr, the XRD method cannot characterize dislocation density in sub-grain and grain boundaries with disorientations larger than ~0.5°. For this reason, the mWA XRD method underestimates the total dislocation density. Finally, (iv) the Tabor's relation remains an empirical law whose coefficient depends on the material.

- Microstructural evolution

Taking into account the evolution of the presented microstructural indicators, only the variation in SSDs and GNDs with a disorientation <0.5° seem to be responsible for the evolution of cladding hardness during the manufacturing process.

4. Conclusions

The Fe-14Cr-1W-0.3Ti-0.3Y$_2$O$_3$ grade developed at CEA exhibits high microstructure stability when being manufactured. The nano-oxide reinforcement obtained with the Y$_2$O$_3$ content, higher than 0.25 wt.%, limits the grain recrystallization. Stability of the microstructure persists up to 1200 °C. For an industrial shaping route, this particularity must be taken into account.

Only slight variations are noticed in all the studied microstructure indicators such as grain size, nano-oxide coalescence, texture and GND density. Hardness evolves as expected, according to heat treatments and deformation stages, while remaining around at 400 HV_1 such as to avoid cracking. Moreover, hardness decrease is mostly controlled by the heat

treatment temperature, and not by its holding time. In this way, shorter heat treatments can be envisaged.

By using a synchrotron X-ray, peak narrowing has been quantified. SSD variation in such a highly deformed BCC alloy has been identified to offer a major contribution to the measured hardness variations through thermomechanical steps.

References

1. DOENE (USDOE Office of Nuclear Energy, Science and Technology (NE)). *A Technology Roadmap for Generation IV Nuclear Energy Systems*; GIF-002-00, 859029; DOENE: Washington, DC, USA, 2002.
2. Carré, F.; Yvon, P.; Chaix, P. Innovative Reactor Systems and Requirements for Structural Materials. In Proceedings of the Workshop Proceedings of the Structural Materials for Innovative Nuclear Systems, Karlsruhe, Germany, 4–6 June 2008; pp. 39–47.
3. Yvon, P.; Carré, F. Structural Materials Challenges for Advanced Reactor Systems. *J. Nucl. Mater.* **2009**, *385*, 217–222. [CrossRef]
4. Huet, J.-J. Possible Fast-Reactor Canning Material Strenghtened and Stabilized by Dispersion. *Powder Metall.* **1967**, *10*, 208–215. [CrossRef]
5. Narita, T.; Ukai, S.; Kaito, T.; Ohtsuka, S.; Kobayashi, T. Development of Two-Step Softening Heat Treatment for Manufacturing 12Cr-ODS Ferritic Steel Tubes. *J. Nucl. Sci. Technol.* **2004**, *41*, 1008–1012. [CrossRef]
6. De Bremaecker, A. Past Research and Fabrication Conducted at SCK●CEN on Ferritic ODS Alloys Used as Cladding for FBR's Fuel Pins. *J. Nucl. Mater.* **2012**, *428*, 13–30. [CrossRef]
7. Toualbi, L.; Olier, P.; Rouesne, E.; Bossu, D.; de Carlan, Y. On the Influence of Cold Rolling Parameters for 14CrW-ODS Ferritic Steel Claddings. *KEM* **2013**, *554–557*, 118–126. [CrossRef]
8. Massey, C.P.; Edmondson, P.D.; Gussev, M.N.; Mao, K.; Gräning, T.; Nizolek, T.J.; Maloy, S.A.; Sornin, D.; De Carlan, Y.; Dryepondt, S.N.; et al. Insights from Microstructure and Mechanical Property Comparisons of Three Pilgered Ferritic ODS Tubes. *Mater. Des.* **2022**, *213*, 110333. [CrossRef]
9. Kim, Y.C.; Jin, H.J.; Noh, S.H.; Kang, S.H.; Choi, B.K.; Kim, K.B.; Kim, G.E.; Kim, T.K. Microhardness and Microstructure of Ferritic-Martensitic ODS Steel Tube Fabricated by a Pilger Process. In Proceedings of the Transactions of the Korean Nuclear Society Spring Meeting, Jeju, Republic of Korea, 11–13 May 2016.
10. Aghamiri, S.M.S; Sowa, T.; Ukai, S.; Oono, N.; Sakamoto, K.; Yamashita, S. Microstructure and Texture Evolution and Ring-Tensile Properties of Recrystallized FeCrAl ODS Cladding Tubes. *Mater. Sci. Eng. A* **2020**, *771*, 138636. [CrossRef]
11. Parida, P.K.; Dasgupta, A.; Sinha, S.K. Comparison of Microstructure and Microtexture Evolution in 9Cr and 18Cr Oxide Dispersion-Strengthened Steels during Fuel Clad Tube Fabrication. *J. Mater. Eng. Perform.* **2021**, *30*, 9227–9236. [CrossRef]
12. Inoue, M.; Kaito, T.; Ohtsuka, S. Research and Development of Oxide Dispersion Strengthened Ferritic Steels for Sodium Cooled Fast Breeder Reactor Fuels. In *Materials Issues for Generation IV Systems*; Ghetta, V., Gorse, D., Mazière, D., Pontikis, V., Eds.; NATO Science for Peace and Security Series B: Physics and Biophysics; Springer: Dordrecht, The Netherlands, 2008; pp. 311–325, ISBN 978-1-4020-8421-8.

13. Alamo, A.; Regle, H.; Pons, G.; Béchade, J.L. Microstructure and Textures of Ods Ferritic Alloys Obtained by Mechanical Alloying. *MSF* **1992**, *88–90*, 183–190. [CrossRef]

14. Ukai, S.; Nishida, T.; Okada, H.; Okuda, T.; Fujiwara, M.; Asabe, K. Development of Oxide Dispersion Strengthened Ferritic Steels for FBR Core Application, (I): Improvement of Mechanical Properties by Recrystallization Processing. *J. Nucl. Sci. Technol.* **1997**, *34*, 256–263. [CrossRef]

15. Ukai, S.; Nishida, T.; Okuda, T.; Yoshitake, T. Development of Oxide Dispersion Strengthened Steels for FBR Core Application, (II): Morphology Improvement by Martensite Transformation. *J. Nucl. Sci. Technol.* **1998**, *35*, 294–300. [CrossRef]

16. Fournier, B.; Steckmeyer, A.; Rouffie, A.-L.; Malaplate, J.; Garnier, J.; Ratti, M.; Wident, P.; Ziolek, L.; Tournie, I.; Rabeau, V.; et al. Mechanical Behaviour of Ferritic ODS Steels—Temperature Dependancy and Anisotropy. *J. Nucl. Mater.* **2012**, *430*, 142–149. [CrossRef]

17. Narita, T.; Ukai, S.; Leng, B.; Ohtsuka, S.; Kaito, T. Characterization of Recrystallization of 12Cr and 15Cr ODS Ferritic Steels. *J. Nucl. Sci. Technol.* **2013**, *50*, 314–320. [CrossRef]

18. Leng, B.; Ukai, S.; Sugino, Y.; Tang, Q.; Narita, T.; Hayashi, S.; Wan, F.; Ohtsuka, S.; Kaito, T. Recrystallization Texture of Cold-Rolled Oxide Dispersion Strengthened Ferritic Steel. *ISIJ Int.* **2011**, *51*, 951–957. [CrossRef]

19. Autones, L.; Aubry, P.; Ribis, J.; Leguy, H.; Legris, A.; de Carlan, Y. Assessment of Ferritic ODS Steels Obtained by Laser Additive Manufacturing. *Materials* **2023**, *16*, 2397. [CrossRef]

20. Allen, A.J.; Zhang, F.; Kline, R.J.; Guthrie, W.F.; Ilavsky, J. NIST Standard Reference Material 3600: Absolute Intensity Calibration Standard for Small-Angle X-ray Scattering. *J Appl Crystallogr* **2017**, *50*, 462–474. [CrossRef]

21. Spartacus, G.; Malaplate, J.; De Geuser, F.; Sornin, D.; Gangloff, A.; Guillou, R.; Deschamps, A. Nano-Oxide Precipitation Kinetics during the Consolidation Process of a Ferritic Oxide Dispersion Strengthened Steel. *Scr. Mater.* **2020**, *188*, 10–15. [CrossRef]

22. Deschamps, A.; De Geuser, F. On the Validity of Simple Precipitate Size Measurements by Small-Angle Scattering in Metallic Systems. *J. Appl. Crystallogr.* **2011**, *44*, 343–352. [CrossRef]

23. Gerold, V.; Kostorz, G. Small-Angle Scattering Applications to Materials Science. *J. Appl. Crystallogr.* **1978**, *11*, 376–404. [CrossRef]

24. Dumont, M.; Commin, L.; Morfin, I.; DeGeuser, F.; Legendre, F.; Maugis, P. Chemical Composition of Nano-Phases Studied by Anomalous Small-Angle X-ray Scattering: Application to Oxide Nano-Particles in ODS Steels. *Mater. Charact.* **2014**, *87*, 138–142. [CrossRef]

25. Ungár, T.; Borbély, A. The Effect of Dislocation Contrast on X-ray Line Broadening: A New Approach to Line Profile Analysis. *Appl. Phys. Lett.* **1996**, *69*, 3173–3175. [CrossRef]

26. Zhang, H.; Johansson, B.; Vitos, L. *Ab Initio* Calculations of Elastic Properties of Bcc Fe-Mg and Fe-Cr Random Alloys. *Phys. Rev. B* **2009**, *79*, 224201. [CrossRef]

27. Borbély, A. The Modified Williamson-Hall Plot and Dislocation Density Evaluation from Diffraction Peaks. *Scr. Mater.* **2022**, *217*, 114768. [CrossRef]

28. Borbély, A.; Aoufi, A.; Becht, D. X-ray Methods for Strain Energy Evaluation of Dislocated Crystals. *J. Appl. Crystallogr.* **2023**, *56*, 254–262. [CrossRef]

29. Hull, D.; Bacon, D.J. *Introduction to Dislocations*, 5th ed.; Elsevier: Amsterdam, The Netherlands; Butterworth Heinemann: Heidelberg, Germany, 2011; ISBN 978-0-08-096672-4.

30. Okuda, T.; Fujiwara, M. Dispersion Behaviour of Oxide Particles in Mechanically Alloyed ODS Steel. *J. Mater. Sci. Lett.* **1995**, *14*, 1600–1603. [CrossRef]

31. Ribis, J.; de Carlan, Y. Interfacial Strained Structure and Orientation Relationships of the Nanosized Oxide Particles Deduced from Elasticity-Driven Morphology in Oxide Dispersion Strengthened Materials. *Acta Mater.* **2012**, *60*, 238–252. [CrossRef]

32. Spartacus, G.; Malaplate, J.; De Geuser, F.; Mouton, I.; Sornin, D.; Perez, M.; Guillou, R.; Arnal, B.; Rouesne, E.; Deschamps, A. Chemical and Structural Evolution of Nano-Oxides from Mechanical Alloying to Consolidated Ferritic Oxide Dispersion Strengthened Steel. *Acta Mater.* **2022**, *233*, 117992. [CrossRef]

33. Zhong, S.Y.; Ribis, J.; Klosek, V.; De Carlan, Y.; Lochet, N.; Ji, V.; Mathon, M.H. Study of the Thermal Stability of Nanoparticle Distributions in an Oxide Dispersion Strengthened (ODS) Ferritic Alloys. *J. Nucl. Mater.* **2012**, *428*, 154–159. [CrossRef]

34. Humphreys, F.J.; Hatherly, M. *Recrystallization and Related Annealing Phenomena*; Elsevier Science: Amsterdam, The Netherlands, 2012; ISBN 978-0-08-098388-2.

35. Serrano, M.; García-Junceda, A.; Hernández, R.; Mayoral, M.H. On Anisotropy of Ferritic ODS Alloys. *Mater. Sci. Technol.* **2014**, *30*, 1664–1668. [CrossRef]

36. Ukai, S.; Mizuta, S.; Yoshitake, T.; Okuda, T.; Fujiwara, M.; Hagi, S.; Kobayashi, T. Tube Manufacturing and Characterization of Oxide Dispersion Strengthened Ferritic Steels. *J. Nucl. Mater.* **2000**, *283–287*, 702–706. [CrossRef]

37. Raabe, D.; Lücke, K. Rolling and Annealing Textures of BCC Metals. *MSF* **1994**, *157–162*, 597–610. [CrossRef]

38. Kestens, L.A.I.; Pirgazi, H. Texture Formation in Metal Alloys with Cubic Crystal Structures. *Mater. Sci. Technol.* **2016**, *32*, 1303–1315. [CrossRef]

39. Pantleon, W. Resolving the Geometrically Necessary Dislocation Content by Conventional Electron Backscattering Diffraction. *Scr. Mater.* **2008**, *58*, 994–997. [CrossRef]

40. Ashby, M.F. The Deformation of Plastically Non-Homogeneous Materials. *Philos. Mag.* **1970**, *21*, 399–424. [CrossRef]

41. Field, D.P.; Trivedi, P.B.; Wright, S.I.; Kumar, M. Analysis of Local Orientation Gradients in Deformed Single Crystals. *Ultramicroscopy* **2005**, *103*, 33–39. [CrossRef]

42. Kocks, U.F.; Argon, A.S.; Ashby, M.F. *Thermodynamics and Kinetics of Slip*; Pergamon Press: Oxford, UK, 1975.

43. Fribourg, G.; Bréchet, Y.; Deschamps, A.; Simar, A. Microstructure-Based Modelling of Isotropic and Kinematic Strain Hardening in a Precipitation-Hardened Aluminium Alloy. *Acta Mater.* **2011**, *59*, 3621–3635. [CrossRef]

44. Tabor, D. *The Hardness of Metals*; Oxford Classic Texts in the Physical Sciences; Oxford University Press: Oxford, UK; Clarendon Press: New York, NY, USA, 2000; ISBN 978-0-19-850776-5.

45. Cahoon, J.R.; Broughton, W.H.; Kutzak, A.R. The Determination of Yield Strength from Hardness Measurements. *Metall. Trans.* **1971**, *2*, 1979–1983. [CrossRef]

46. Lacy, C.E.; Gensamer, M. The Tensile Properties of Alloyed Ferrites. *Trans. Am. Soc. Met.* **1944**, *32*, 88–110.

47. Martin, J.W. *Micromechanisms in Particle-Hardened Alloys*; Cambridge University Press: Cambridge, UK, 1980; ISBN 0-521-22623-6.

48. Dangwal, S.; Edalati, K.; Valiev, R.Z.; Langdon, T.G. Breaks in the Hall–Petch Relationship after Severe Plastic Deformation of Magnesium, Aluminum, Copper, and Iron. *Crystals* **2023**, *13*, 413. [CrossRef]

49. Srinivasarao, B.; Oh-Ishi, K.; Ohkubo, T.; Hono, K. Bimodally Grained High-Strength Fe Fabricated by Mechanical Alloying and Spark Plasma Sintering. *Acta Mater.* **2009**, *57*, 3277–3286. [CrossRef]

50. Kubin, L.P.; Mortensen, A. Geometrically Necessary Dislocations and Strain-Gradient Plasticity: A Few Critical Issues. *Scr. Mater.* **2003**, *48*, 119–125. [CrossRef]

51. Ateba Betanda, Y.; Helbert, A.-L.; Brisset, F.; Mathon, M.-H.; Waeckerlé, T.; Baudin, T. Measurement of Stored Energy in Fe–48%Ni Alloys Strongly Cold-Rolled Using Three Approaches: Neutron Diffraction, Dillamore and KAM Approaches. *Mater. Sci. Eng. A* **2014**, *614*, 193–198. [CrossRef]

52. Birosca, S.; Liu, G.; Ding, R.; Jiang, J.; Simm, T.; Deen, C.; Whittaker, M. The Dislocation Behaviour and GND Development in a Nickel Based Superalloy during Creep. *Int. J. Plast.* **2019**, *118*, 252–268. [CrossRef]

53. Zhu, C.; Harrington, T.; Gray, G.T.; Vecchio, K.S. Dislocation-Type Evolution in Quasi-Statically Compressed Polycrystalline Nickel. *Acta Mater.* **2018**, *155*, 104–116. [CrossRef]

54. Wilkens, M. *Fundamental Aspects of Dislocation Theory*; Simmons, J.A., de Wit, R., Bullough, R., Eds.; National Bureau of Standards Special Publication 317; U. S. Government Printing Office: Washington, DC, USA, 1970; Volume 2.

55. Ridley, N.; Stuart, H. Lattice Parameter Anomalies at the Curie Point of Pure Iron. *J. Phys. D Appl. Phys.* **1968**, *1*, 1291–1295. [CrossRef]

56. Kozlov, E.V.; Koneva, N.A. Internal Fields and Other Contributions to Flow Stress. *Mater. Sci. Eng. A* **1997**, *234–236*, 982–985. [CrossRef]

57. Mughrabi, H. The α-Factor in the Taylor Flow-Stress Law in Monotonic, Cyclic and Quasi-Stationary Deformations: Dependence on Slip Mode, Dislocation Arrangement and Density. *Curr. Opin. Solid State Mater. Sci.* **2016**, *20*, 411–420. [CrossRef]